Winds of Stars and Exoplanets
Proceedings IAU Symposium No. 370, 2023
A. A. Vidotto, L. Fossati & J. S. Vink, eds.
doi:10.1017/S1743921323000108

Observations of outflows of massive stars

Andrea Mehner

ESO - European Organisation for Astronomical Research in the Southern Hemisphere, Alonso de Cordova 3107, Vitacura, Santiago de Chile, Chile

Abstract. Mass loss plays a key role in the evolution of massive stars and their environment. High mass-loss events are traced by complex circumstellar ejecta and intricate line profiles across the upper Hertzsprung-Russell diagram for massive stars in different evolutionary stages. The basic physics of radiation-driven stellar wind for hot stars is well understood. However, the driving mechanisms and related instabilities for their enhanced mass-loss episodes and the driving mechanisms for the mass loss of cool stars are still debated. In this review, the mass-loss characteristics and the possible mechanisms will be surveyed for an observational set of prominent massive stellar populations that experience outflows, strong stellar winds, and periods of enhanced and eruptive mass loss; massive young stellar objects, OB-type stars, red supergiants, warm hypergiants, luminous blue variables, and Wolf-Rayet stars.

Keywords. stars: emission-line, Be, stars: evolution, (stars:) circumstellar matter, stars: winds, outflows, stars: variables: other

1. Introduction

The outflows of massive stars play a crucial role in the dynamics and chemical evolution of galaxies. They are key contributors to the turbulence budget and chemical enrichment of the interstellar medium, influencing directly and indirectly the star formation rate and efficiency. The mass-loss rates of massive stars determine their evolution, death, and end-product, yielding the observed diversity of evolved massive stars and of supernovae (SNe).

Mass loss of massive stars includes steady stellar winds and enhanced and eruptive mass-loss episodes. This is manifested in their complex circumstellar environments. Material in the form of molecular, atomic, and ionized gas, and dust can be seen in a variety of geometries, e.g., as arcs, collimated outflows, latitude dependent mass-loss geometries with equatorial density enhancements ("disks"), and large-scale circumstellar nebulae. Current observational efforts to characterize massive star outflows focus on their driving mechanisms, outflow rates, underlying fundamental physical and chemical processes that include the instabilities and triggers that can result in enhanced or eruptive mass-loss behavior, and the dependency on metallicity, rotation, and binarity.

At high effective temperatures, corresponding to OB-type stars, the dominant physical process resulting in steady mass loss is radiative acceleration (Kudritzki & Puls 2000; Puls et al. 2008; Vink 2021). Metal ions, such as Fe, are efficient photon absorbers at specific line frequencies, resulting in radiative acceleration (Lucy & Solomon 1970; Castor et al. 1975). Line driven winds in lower metallicity (Z) environments are predicted to be much weaker, with lower mass-loss rates. Bi-stability jumps may exist at specific temperatures where changes in the wind ionization occur (Vink et al. 2001; Petrov et al. 2016; Björklund et al. 2021). Some of the observed very strong mass-loss events may only be explained by continuum-driven winds or explosions. The mass-loss mechanism

operational among the cooler post-main sequence super- and hypergiants, which can also exhibit enhanced and eruptive mass-loss behavior, is debated. Radiation pressure on dust grains or molecules, aided by pulsation or convection and additionally enhanced by magnetic phenomena can all be invoked.

Measured mass-loss rates are subject to systematic uncertainties and each mass-loss diagnostic has its own limitation. For example, Hα recombination emission (Puls et al. 1996) is sensitive to wind clumping (Fullerton et al. 2006) and limited to relatively high mass-loss rates. Ultraviolet (UV) P Cygni resonance lines (Lamers et al. 1995) are less sensitive to clumping but require access to UV satellites, while X-ray light curves and spectroscopy provide excellent information but only for close binary systems. Huge progress has been made in the past decade by applying non-LTE stellar atmosphere codes such as CMFGEN (Hillier & Miller 1998), PoWR (Gräfener et al. 2002; Sander et al. 2017), and FASTWIND (Puls et al. 2005) to fit stellar spectra and spectral energy distributions (SEDs) for a broad wavelength range to derive stellar and wind parameters. Many studies with new infrared to radio instrumentation were conducted to derive wind, and circumstellar gas and dust parameters around massive stars. Other methods include observations of masers (Habing 1996), bow-shocks (Kobulnicky et al. 2019; Henney & Arthur 2019), and spatially resolved circumstellar nebulae using a variety of techniques, including infrared interferometry (Monnier et al. 2004).

1.1. *Massive stars and exoplanets*

Exoplanets are very common around cool stars (Dressing & Charbonneau 2013), but studies failed to detect giant planets around stars with more than 3 $M_{\odot}$ (Reffert et al. 2015).† This led to the idea that giant planet formation or inward migration is suppressed around higher-mass stars. The increased radiation field from a hotter star results in short disk lifetimes, making planet formation and/or growth much less likely. In addition, any newborn planets would be susceptible to radiation stripping from the hot star and undergo atmosphere evaporation (e.g., Poppenhaeger et al. 2021).

Nonetheless, the discovery of the planet b Cen (AB)b showed that stars and stellar systems up to at least $6-10$ $M_{\odot}$ can host giant planets on wide orbits (Janson et al. 2021). High-contrast direct imaging observations with the Spectro-Polarimetric High-contrast Exoplanet REsearch instrument (SPHERE), mounted on the Very Large Telescope (VLT) at the European Southern Observatory (ESO), revealed a planet about ten times more massive than Jupiter in a wide circumbinary orbit around the b Cen stellar system. The planet orbits at 100 times the Jupiter-Sun distance, one of widest planet orbits discovered yet. The large distance could be key to the planet's survival in this extreme stellar environment. The more massive star in the binary has the spectral type B2.5V, corresponding to an effective temperature of $\sim 18\,000$ K. Its strong UV radiation make it doubtful that the planet could have formed in-situ by the core-accretion process. Instead, it may have been captured by the stellar system after forming in isolation, or the planet could have formed rapidly from the circumstellar gas disk through gravitational instability.

VLT SPHERE high-contrast near-infrared images and integral field spectra have enabled further discoveries, demonstrating that AO-assisted coronagraphic surveys can place constraints on the multiplicity properties of massive star companions. First results indicate that the companion mass function is populated down to the lowest stellar masses.

† The first exoplanets were discovered around millisecond radio pulsars, i.e., rapidly rotating neutron stars. However, this does not imply these planets were formed around their massive progenitor stars as they would likely be ablated or unbound during stellar death. More likely, these planets originated in the SN fallback disk around the newly-formed neutron star or from a disk of a disrupted binary companion.

https://doi.org/10.1017/S1743921323000108 Published online by Cambridge University Press

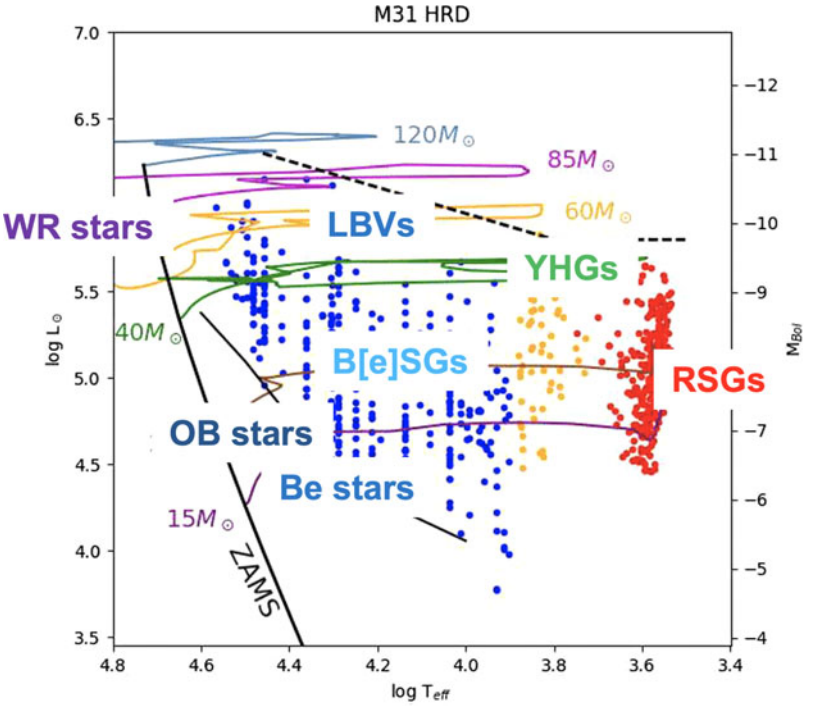

Figure 1. Representative HR diagram of the selected massive star populations (Figure from Humphreys et al. 2017, annotated).

Squicciarini et al. (2022) found that the massive star μ^2 Sco ($M \sim 9\ M_\odot$) has a substellar companion ($14.4 \pm 0.8\ M_J$) at a projected separation of 290 ± 10 au, and a probable second similar object ($18.5 \pm 1.5\ M_J$) at 21 ± 1 au. These companions are slightly more massive than the deuterium-burning limit, but they may still have formed under a planet-like scenario. Reggiani et al. (2022) probed the low-mass end of the companion mass function for 18 O-type stars and found five objects at the stellar/substellar mass boundary with estimated masses $< 0.25\ M_\odot$.

2. Science highlights of selected massive star populations

The upper Hertzsprung-Russell (HR) diagram is populated by a diverse group of luminous, and variable massive stars. Many of them show evidence for strong stellar winds and periods of enhanced or eruptive mass loss. Despite extensive observing campaigns and many theoretical studies over the past decades to investigate these massive stars, there are still many challenges to our understanding of their evolution and their final fate. This is because of low-number statistics and the variety and complexity of the involved physics, such as the impact of metallicity, mass-loss history, rotation, and binarity. In the following, recent observational science highlights for selected massive star populations (Figure 1) are presented to shine a light on the diversity of observations of outflows in massive stars and the diversity of the physical processes involved.

2.1. *Massive young stellar objects*

Massive Young Stellar Objects (MYSOs) are embedded in their dense molecular birth clouds. They are defined as infrared-bright objects that have an SED that peaks at ~ 100 μm and a total luminosity $> 10^4$ $L_\odot$. Collimated outflows occur in most

https://doi.org/10.1017/S1743921323000108 Published online by Cambridge University Press

astrophysical systems in which accretion, rotation, and magnetic fields interact and they are a fundamental aspect of star formation (Bally 2016). Outflows from forming stars have a profound impact on their surrounding clouds. The outflow mass directly launched by a protostar is estimated to be about $10-30\%$ of the accreted gas, i.e., $10-30\%$ of the final stellar mass. Jets and winds create cavities and inject energy and momentum on a wide-range of lengths from less than 0.01 pc to over 30 pc, which may dominate the generation of turbulence and cloud motions and determine the final stellar masses (Rosen & Krumholz 2020). As an example, Xu et al. (2022) adopted the deep learning method CASI-3D to systemically identify protostellar outflows in Orion in ^{12}CO and ^{13}CO observations obtained with the Nobeyama Radio Observatory 45m telescope (NRO 45m). They found a total outflow mass of 6332 $M_{\odot}$ and total kinetic energy of 6×10^{47} erg, sufficient to maintain the level of turbulence against dissipation in the Orion molecular cloud. The terminal shocks in outflows can dissociate molecules, sputter grains, and alter the chemical composition of the impacted media.

Protostellar outflows can be observed at radio to X-ray wavelengths in the continuum and a multitude of spectral lines (Bally 2016). Near- and mid-infrared observations and aperture synthesis with centimeter- and millimeter-wave interferometers are enabling outflow studies of highly obscured objects. The youngest outflows are best traced by molecules such as CO, SiO, H_2O, and H_2, while older outflows are best traced by shock-excited atoms and ions such as hydrogen-recombination lines, [S II], and [O II]. The outflows record the mass-accretion histories of forming stars and their symmetries provide clues about the dynamical environment of the engine. Variations in ejection velocity, mass-loss rate, and flow orientation provide information on the protostar-disk system and potential companions. For example, S- and Z-shaped symmetries indicate that the outflow axis has changed over time, maybe due to precession induced by a companion. C-shaped symmetries indicate a relative motion between the star and surrounding medium. The more luminous the source, the less collimated the outflow. Most YSOs indicating spectral type B or later (luminosities of 10^{-1} to 10^{-2} $L_{\odot}$) tend to have outflows that are highly collimated. MYSOs with luminosities of $L \sim 10^5$ $L_{\odot}$ or higher become the most massive early O-type stars. Their outflows are frequently poorly collimated.

Orion-Kleinmann-Low nebula. The Orion Nebula is the nearest site of ongoing and recent massive star formation. A powerful and poorly collimated outflow emerges from the Orion-Kleinmann-Low nebula in the Orion Molecular Cloud. Many observations have confirmed a link between this outflow and an explosive event. Explanations for the explosive outflow range from a "magnetic bomb" (Matt et al. 2006) to the release of gravitational potential energy associated with the formation of a compact binary or stellar mergers (Bally & Zinnecker 2005).

AO near-infrared images obtained with the Gemini South multi-conjugate AO system (GeMS) and near-infrared imager (GSAOI), combined with previous observations, were used to study the proper motion of the high-velocity H_2 knots and three ejected stars (Bally et al. 2015, 2020) (Figure 2). The results are consistent with an origin within a few au of a massive star and a multi-body dynamic encounter that ejected the Becklin-Neugebauer object and radio source I about 500 yr ago. ALMA observations show a roughly spherically symmetric distribution of over a hundred ^{12}CO streamers with velocities extending from -150 km s^{-1} to $+145$ km s^{-1}, indicating again a dynamic age of ~ 500 yr and allowing the identification of the explosion center (Bally et al. 2017).

2.2. *OB dwarfs, giants, supergiants*

Some OB-type stars show evidence for strong winds and circumstellar material, indicating additional mass-loss drivers to their steady radiation-driven stellar winds. For

https://doi.org/10.1017/S1743921323000108 Published online by Cambridge University Press

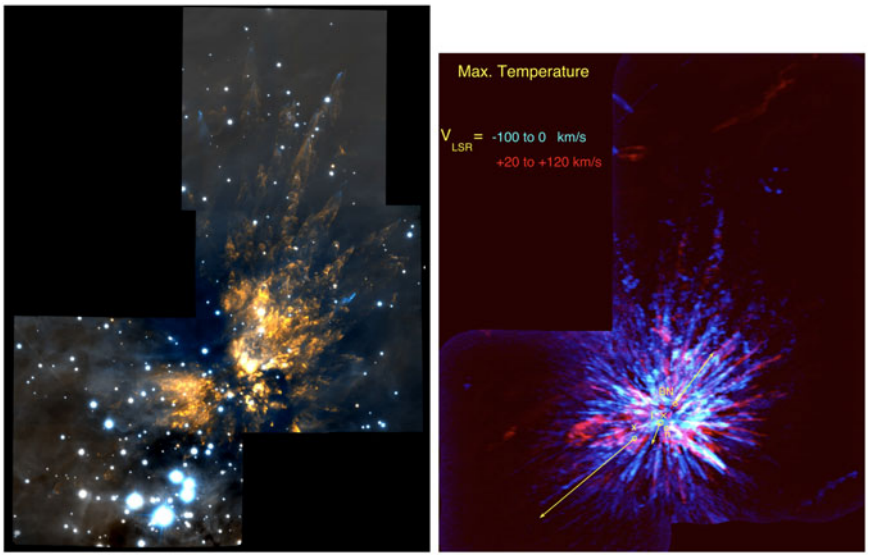

Figure 2. Explosive outflow from the Orion-Kleinmann-Low nebula in the Orion Molecular Cloud. Left: Combined H_2 (orange), [Fe II] (cyan), and K color GSAOI image (Figure from Bally et al. 2015). Right: CO $J = 2 - 1$ ALMA image (Figure from Bally et al. 2020).

example, the Be stars and B[e] supergiants (B[e]SGs) have strong and time-variable emission lines and show evidence for disk-like circumstellar material.

Be stars have ionized gaseous disks, which have been explained with the viscous decretion disk model (Rivinius et al. 2013). The mass-ejection process is likely linked to non-radial pulsation and small-scale magnetic fields, which act on top of a fast stellar rotation rate of $> 75\%$ of critical. Based on infrared observations obtained with *IRAS*, *AKARI*, and *AllWISE*, disk mass decretion rates have been estimated to be between 10^{-12} $M_\odot$ yr^{-1} and 10^{-9} $M_\odot$ yr^{-1} (Vieira et al. 2017).

B[e]SGs display outflows with a hot, fast (~ 1000 km s^{-1}) line-driven polar wind and a cool, slow (~ 100 km s^{-1}), dense equatorial wind (Zickgraf et al. 1985). Infrared excess from dust is indicative of a hot circumstellar dust disk or torus. The fast wind in the polar region is similar to the winds of normal blue supergiants. Imaging and interferometry have spatially resolved the environment of the closest and brightest Galactic B[e]SGs, providing precise measurements of the disk inclinations and disk sizes (e.g., Domiciano de Souza et al. 2007, 2008; Wheelwright et al. 2012). The kinematics of the equatorial gaseous material favor Keplerian rotation (Kraus et al. 2007, 2010; Millour et al. 2011; Wheelwright et al. 2012), likely accumulated in multiple, partial rings and possible spiral arm-like structures (Aret et al. 2012; Kraus et al. 2016; Maravelias et al. 2018). Several B[e]SGs have been discovered to be in short-period binary systems and the dynamical and spatial information indicates that the prevalent geometry is a circumbinary ring or disk (Kraus et al. 2013; Porter et al. 2022). Large dust shell structures and nebulae are detected around some objects, hinting at major mass-loss events (Liimets et al. 2022). Dust formation in the winds of hot stars is generally inhibited by the low particle densities and the harsh UV environment and thus the formation and continuous presence of the circumstellar dusty disks around the hot B[e]SGs are intriguing. Different disk formation scenarios could lead to the B[e] phenomenon, but binarity and mergers are preferred for several objects.

https://doi.org/10.1017/S1743921323000108 Published online by Cambridge University Press

High-resolution, multi-wavelength, multi-epoch surveys of hundreds of Galactic and extra-galactic O- and B-type stars have been analyzed during the past decade with several stellar atmosphere codes to infer their stellar and wind parameters in a consistent manner, leading to major progress in our understanding of the mass loss in OB-type stars. Mokiem et al. (2006) and Mokiem et al. (2007b) studied optical spectra of 31 O- and early B-type stars in the Small and Large Magellanic Clouds (SMC, LMC) obtained with the Fibre Large Array Multi Element Spectrograph (FLAMES) at the VLT. Stellar parameters were determined using the stellar atmosphere code FASTWIND. One of the most important recent projects on OB-stars has been the VLT-FLAMES Tarantula Survey with multi-epoch optical spectroscopy of over 800 massive stars in the 30 Doradus region of the LMC (Evans et al. 2011). Bestenlehner et al. (2014) performed a spectral analysis of optical and near-infrared data using the non-LTE radiative transfer code CMFGEN to obtain the stellar and wind parameters of 62 O, Of, Of/WN, and WNh stars. Ramírez-Agudelo et al. (2017) determined stellar, photospheric, and wind properties of 72 presumably single O-type giants and supergiants with the non-LTE stellar atmosphere model FASTWIND. Ramachandran et al. (2019) reported a spectroscopic study of massive stars of spectral types O (23 stars) and B (297 stars) in the SMC, using observations with VLT FLAMES and archival UV data. The spectra were analyzed using PoWR stellar atmosphere models. Bouret et al. (2021) studied the evolutionary and physical properties of 13 SMC O-type giants and supergiants, using UV spectra obtained with the *Hubble Space Telescope's (HST) Cosmic Origins Spectrograph (COS)* and *Space Telescope Imaging Spectrograph (STIS)*, supplemented by optical spectra. The stellar atmosphere code CMFGEN was used to derive photospheric and wind properties. Mass-loss rates were derived from the analysis of UV P Cygni profiles of C IV and S IV resonance doublets, plus the Hα line for stars with optical spectra. The β exponent of the wind velocity law was derived from the fit of the shape of the P Cygni profile. Clumping parameters, f and v_{cl}, were derived in the UV domain. Marcolino et al. (2022) investigated the wind properties of massive stars in the Galaxy and SMC. They derived an empirical Z dependence from CMFGEN models for the winds of 96 O and B-type stars. Rickard et al. (2022) obtained UV and optical spectra of a sample of 19 O-type stars within NGC 346 in the SMC and used the non-local thermal equilibrium model atmosphere code PoWR to determine wind parameters and ionising fluxes to study stellar winds at low metallicity. Rubio-Díez et al. (2022) probed the radial clumping stratification of 25 OB stars in the intermediate and outer wind regions to derive upper limits for mass-loss rates, using optical to radio observations.

Some of the main issues identified in these studies are that the presence of inhomogeinities in the stellar winds of hot, luminous stars ("clumping") leads to severe discrepancies among different mass-loss rate diagnostics, and also between empirical estimates and theoretical predictions. This may require a reassessment of the relative roles of mass loss in steady stellar winds, in eruptive events, and through binary interaction. On the other hand, mass-loss rates inferred for low luminosity O-type stars were found to be much lower than predicted by theory ("weak wind" uncertainty). Wind line variability between observing epochs can lead to differences in the mass-loss rate estimates of up to a factor of three.

There is a strong relationship between the wind momentum and the stellar luminosity. The empirical scaling of $\dot{M} \propto L^{2.4}$, however, is steeper than theoretically expected. Objects in higher metallicity environments are observed to have stronger winds, i.e., the mass loss properties for the LMC are intermediate to massive stars in the Galaxy and SMC. For bright objects ($log\ L/L_{\odot} > 5.4$), the mass-loss rate scales with metallicity as $\dot{M} \propto Z^{0.5-0.8}$. This metallicity dependency seems to get weaker at lower luminosities.

https://doi.org/10.1017/S1743921323000108 Published online by Cambridge University Press

2.3. *Red supergiants*

Red supergiants (RSGs) are evolved, helium-fusing stars originating from stars with initial masses of $8-40\ M_{\odot}$. They are the classical progenitors of Type II-P core-collapse SNe. The defining signature of mass loss in RSGs is the presence of circumstellar dust, observed as excess radiation in their SEDs from the silicate emission features at 10 μm and 20 μm. Several RSGs and red hypergiants show evidence for clumpy winds (e.g., Kervella et al. 2011; Ohnaka 2014; Montargès et al. 2019) and discrete, directed gaseous outflows in their optical and infrared images, spectra, and light curves (Humphreys & Jones 2022).

The driving mechanism of their strong mass loss is not understood, but leading processes are radiation pressure on dust grains or molecules, pulsations, and convective and magnetic activity (Josselin & Plez 2007; Thirumalai & Heyl 2012). The discovery of large-scale surface asymmetries or hot spots on their surfaces, which vary on timescales of months or years, supports convection as an important mechanism (e.g., Monnier et al. 2004; Haubois et al. 2009; Baron et al. 2014). Massive arcs and clumps, discrete gaseous outflows, and the presence of magnetic fields in their ejecta, suggest that enhanced convective activity together with magnetic activity may be important for the high-mass ejections (Humphreys & Jones 2022). However, studies of the atmospheres of RSGs showed that pulsation and convection alone cannot explain the elevation of material to the molecular and dust formation zones (Arroyo-Torres et al. 2015).

Beasor et al. (2020) found that quiescent mass-loss during the RSG phase is not effective at removing a significant fraction of the hydrogen-envelope prior to core-collapse. They measured the mass-loss rates of RSGs via SED modelling using mid-infrared photometry from the Stratospheric Observatory for Infrared Astronomy (SOFIA) Faint Object infraRed CAmera for the SOFIA Telescope (FORCAST) instrument and archival data from several observatories. When comparing their new mass-loss prescription to the treatment of mass-loss currently implemented in evolutionary models, they found models drastically over-predict the total mass loss, by up to a factor of 20. Thus, single stars with initial masses $< 25\ M_{\odot}$ do not lose enough mass through their quiescent winds to evolve blueward, and hence cannot create WR stars, BSGs, or LBVs as some evolutionary models have predicted.

Betelgeuse. The RSG Betelgeuse is a semi-regular variable with a period of ~ 400 d, attributed to radial pulsations, and a longer ~ 2000 d period, associated with convective and magnetic activity. Its mass-loss rate is on the order of a few $10^{-7}\ M_{\odot}\ \mathrm{yr}^{-1}$. High-spatial near- and mid-infrared imaging with the VLT Imager and Spectrometer for mid Infrared (VISIR) revealed that Betelgeuse has several clumps of dusty material within 1 arcsec of the star (Kervella et al. 2011). ALMA observations suggest that convective cells led to the production of these dusty knots and molecular plumes (Kervella et al. 2018).

Betelgeuse showed an unexpected visual dimming event by about 1 mag from November 2019 to March 2020. Spatially resolved UV spectra from *HST STIS* just prior to the event revealed an increase in the UV flux and variations in the Mg II line emission from the chromosphere over the southern hemisphere of the star, supporting an outflow of material from a convective cell that may have been enhanced by the outward motion in its 400 d radial pulsation (Dupree et al. 2020). The outflow expanded and cooled, possibly forming dust causing the deep dimming in the visual light curve. Since Betelgeuse also fainted at submillimeter wavelength, Dharmawardena et al. (2020) questioned that the dimming is due to dust formation and suggested a change in radius or in temperature. Kravchenko et al. (2021) used the tomographic method to a series of high-resolution HERMES observations at the Anglo-Australian Telescope (AAT), which

https://doi.org/10.1017/S1743921323000108 Published online by Cambridge University Press

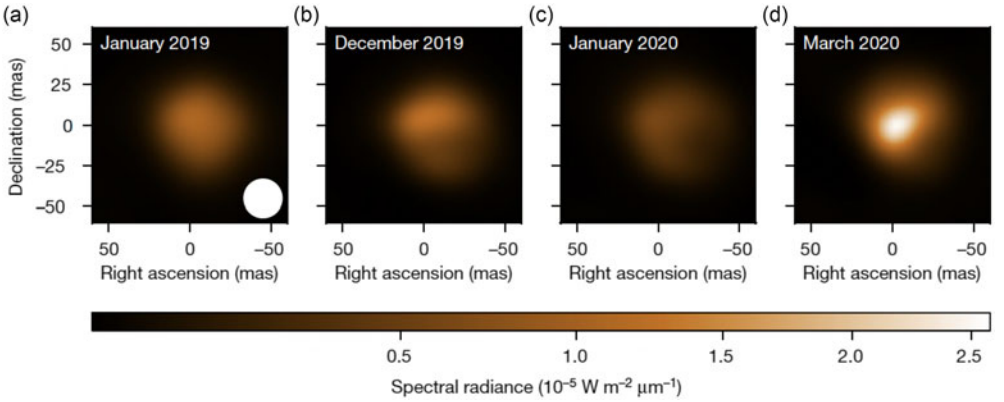

Figure 3. VLT SPHERE observations of the RSG Betelgeuse (Figure from Montargès et al. 2021).

allowed to probe different depths in the stellar atmosphere and to recover the corresponding disk-averaged velocity field. They found that the succession of two shocks along our line-of-sight in February 2018 and January 2019, combined with underlying convection and/or outward motion present at this phase of the 400 d pulsation cycle, produced a rapid expansion of a portion of the atmosphere and an outflow between October 2019 and February 2020. This resulted in a sudden increase in molecular opacity in the cooler upper atmosphere of Betelgeuse and, thus, in the decrease of the star's brightness. A visual spectro-polarimetric image obtained with VLT SPHERE showed a remarkable corresponding fading of its southern hemisphere (Montargès et al. 2021, see Figure 3). A change in diameter was ruled out via VLTI GRAVITY observations. The authors demonstrated that the fading was due to dust formation related to the gaseous outflow from a convective cell. They estimate a total mass associated with the dusty and gaseous outflow of $(0.7-3)\times10^{-7}\ M_{\odot}$. Taniguchi et al. (2022) presented photometry of Betelgeuse with a cadence of about one observations every two days between 2017 and 2021 in the $0.45-13.5\ \mu$m wavelength range obtained by the Himawari-810 geostationary meteorological satellite. By examining also the optical and near-infrared light curves, they showed that both a decreased effective temperature and increased dust extinction may have contributed by almost equal amounts to the Great Dimming.

VY CMa. The red hypergiant VY CMa is one of the most luminous red stars in the Galaxy ($L\sim3\times10^{5}\ L_{\odot}$). The star belongs to a class of evolved massive stars that represent a short-lived evolutionary phase characterized by high mass-loss rates of up to $\sim10^{-4}\ M_{\odot}\ \mathrm{yr}^{-1}$, extensive circumstellar ejecta, asymmetric ejections, and multiple high mass-loss events. Near-infrared spectro-interferometric observations with the Astronomical Multi-BEam combineR (AMBER) at the VLTI showed asymmetric, possibly clumpy, atmospheric layers (Wittkowski et al. 2012). Its current mass is estimated to be $\sim17\ M_{\odot}$ with an initial mass of $25-30\ M_{\odot}$. It is one of the largest RSGs with a stellar radius of $1420\pm120\ R_{\odot}$.

Decin et al. (2006) modelled the line profile of low excitation submillimeter CO lines, observed with the James Clerk Maxwell Telescope (JCMT) and the Swedish-ESO Submillimetre Telescope (SEST), emitted in the circumstellar envelope to study the star's mass-loss history. They demonstrated that this source underwent a phase of high mass loss about 1000 yr ago ($\sim3.2\times10^{-4}\ M_{\odot}\ \mathrm{yr}^{-1}$), which lasted for 100 yr. This phase was preceded by a low mass-loss phase ($\sim1\times10^{-6}\ M_{\odot}\ \mathrm{yr}^{-1}$), which lasted for 800 yr. The current mass-loss rate is on the order of $8\times10^{-5}\ M_{\odot}\ \mathrm{yr}^{-1}$. Mid- and far-infrared observation with SOFIA found no extended cold dust with an age greater than about

https://doi.org/10.1017/S1743921323000108 Published online by Cambridge University Press

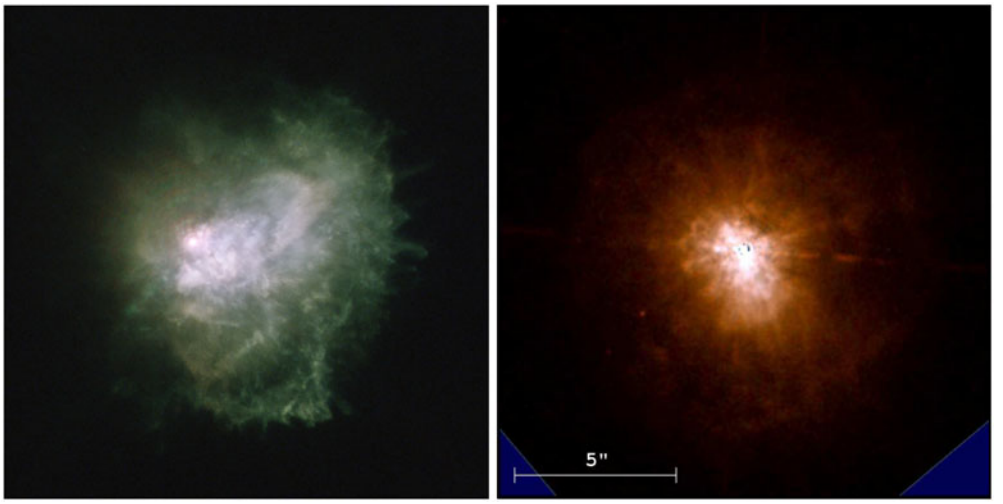

Figure 4. Left: The red hypergiant VY CMa with *HST WFPC2*. Right: The post-RSG IRC +10420 with *HST WFPC2* (Figure from Humphreys et al. 1997).

1200 yr (Shenoy et al. 2013). ALMA submillimeter observations revealed massive, dusty condensations (O'Gorman et al. 2015; Vlemmings et al. 2017; Kamiński 2019), confirming numerous high mass-loss events over the past few hundred years. ALMA gaseous sodium chloride (NaCl) emission of the inner wind shows evidence of localized mass ejections (Decin et al. 2016). Mass estimates of some of the knots and clumps, based on infrared imaging and measurements from ALMA, yield masses on the order of a few 10^{-3} $M_{\odot}$ (Shenoy et al. 2013; O'Gorman et al. 2015; Gordon et al. 2019; Humphreys & Jones 2022).

With *HST Wide Field and Planetary Camera 2 (WFPC2)* images and *STIS* spectra, the orientation and the ejection ages of the complex circumstellar ejecta were determined (Humphreys et al. 2021; Humphreys & Jones 2022, see Figure 4). The closest knots were likely ejected within the past century and one knot as recent as in 1985–1990. The numerous knots to the south and southwest have ejection ages around 120, 200, and 250 yr ago. The random orientation of the ejecta suggests that the mass-loss events are driven by localized, large-scale ejections, maybe due to magnetic and convective regions. Several knot ejection times correspond to periods of the star's photometric variability, which suggests that discrete ejections may be common and large-scale surface or convective activity is a major source of mass loss for RSGs (Humphreys et al. 2021).

2.4. *The warm hypergiants*

Yellow hypergiants (YHGs) are rare, unstable, massive stars (de Jager 1998). They are thought to be progenitors of some SNe. As post-RSGs evolve back to the hot side of the HR diagram, they intersect a temperature domain (the "Yellow Void" or "Yellow Wall") in which their atmospheres become unstable against quasi-periodic pulsations. This can, on timescales of decades, result in episodic mass-loss. Mass-loss rates are on the order of 10^{-4} to 10^{-3} $M_{\odot}$ yr^{-1}, resulting in large, extended circumstellar gas and dust envelopes.

IRC +10420. The YHG or intermediate post-RSG IRC +10420 is a powerful infrared source. In the past 30 yr its apparent spectral type has changed from a late F-type to a mid-A-type, maybe due to its post-RSG evolution to warmer temperatures (Oudmaijer et al. 1996). IRC +10420's infrared SED from SOFIA FORCAST imaging cannot be explained by a single mass-loss rate (Shenoy et al. 2016). During a period

https://doi.org/10.1017/S1743921323000108 Published online by Cambridge University Press

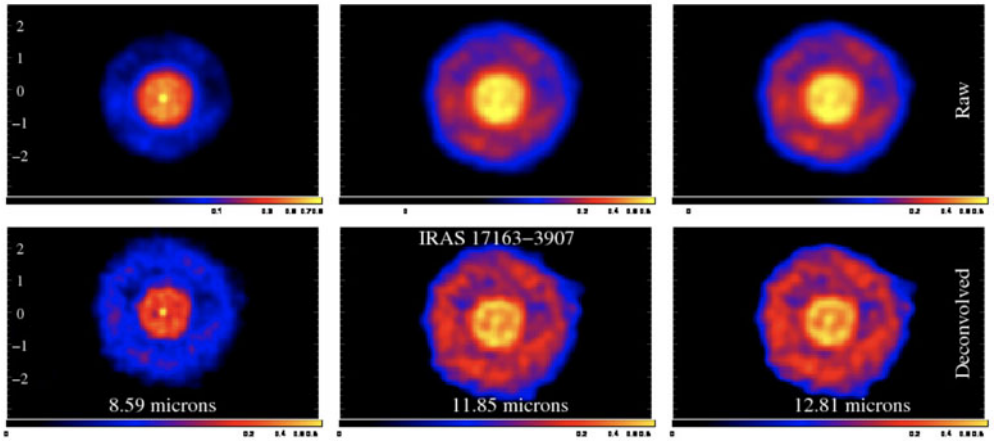

Figure 5. The YHG Fried Egg nebula with VLT VISIR (Figure from Lagadec et al. 2011).

from about 6000 yr to 2000 yr ago, the star likely had a very high mass-loss rate of 2×10^{-3} $M_{\odot}$ yr^{-1}, which then dropped to $\sim 10^{-4}$ $M_{\odot}$ yr^{-1}.

HST WFPC2 optical images revealed a complex asymmetric circumstellar environment, with condensations or knots, ray-like features, and several arcs or loops within 2 arcsec of the star, and distant reflection shells. These features are evidence for high mass-loss episodes during the past few hundred years. The transverse motions of numerous knots, arcs, and condensations in its inner ejecta from second epoch *HST WFPC2* images, combined with the radial motions for several of the features, showed that they were ejected at different times, in different directions, and presumably from separate regions on the surface of the star (Tiffany et al. 2010). Vlemmings et al. (2017) used ALMA observations to study the polarization of SiO thermal/maser lines and dust continuum at 1.7 mm. Emission from magnetically aligned grains is the most likely origin of the observed continuum polarisation, which suggests a strong role of surface activity of a convective nature and magnetic fields in the star's recent mass-loss history. At milliarcsecond spatial resolution, the outflow produced by IRC +10420 has the shape of an hourglass nebula, possibly induced by high rotation and latitude dependent mass-loss (Koumpia et al. 2022).

Fried Egg nebula. One of the more publicized objects is the so-called Fried Egg nebula (IRAS 17163−3907). Huge dusty shells were observed in VLT VISIR images (Lagadec et al. 2011, see Figure 5). The first interpretation, adopting a distance of 4 kpc, was that these shells were caused by successive ejections $\sim$400 yr apart and that the total circumstellar mass exceeded 4 $M_{\odot}$. Using a large set of optical to infrared spectroscopic, photometric, spectropolarimetric, and interferometric data, and adopting the Gaia DR2 distance of 1.2 kpc, Koumpia et al. (2020) identified three distinct mass-loss episodes 30, 100, 125 yr ago, which are characterized by different mass-loss rates and resulting in a total mass lost of 6.5×10^{-3} $M_{\odot}$. The authors argued that the second bi-stability jump at $T_{\rm eff} \sim 8800$ K, due to the recombination of Fe III to Fe II (Petrov et al. 2016), is a promising mechanism for the mass-loss ejections. However, the observations do not allow yet to discriminate between the photospheric pulsations and wind bi-stability mechanisms as the prevalent mass-loss mechanism.

2.5. *Classical and giant eruption LBVs*

Classical LBVs experience "outbursts" and episodes of enhanced mass loss on timescales of years to decades. During an outburst, they transit in the HR diagram

https://doi.org/10.1017/S1743921323000108 Published online by Cambridge University Press

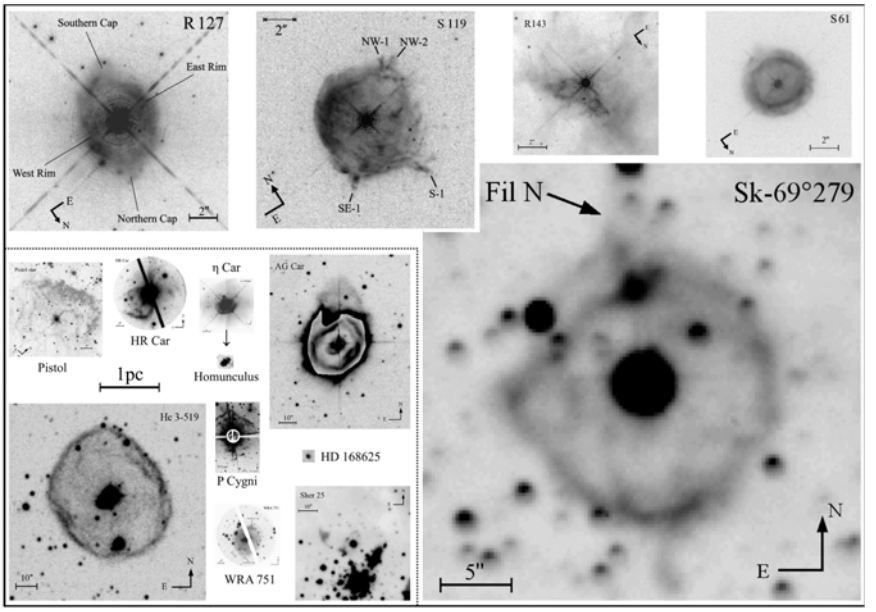

Figure 6. Galactic and LMC LBV nebulae in *HST* images (Figure from Weis 2011).

from a hot quiescent state ($T_{\rm eff} \sim 12\,000 - 30\,000$ K) to lower temperatures ($T_{\rm eff} \sim 7\,000 - 8\,000$ K), i.e., their spectral appearance changes from a hot supergiant to a much cooler A or F-type supergiant. Their visual magnitudes change by $1 - 2$ mag, at almost constant bolometric luminosity. They are generally divided into high-luminous LBVs ($log\ L/L_{\odot} > 5.8$), which evolve from the most massive stars with $M > 50\ M_{\odot}$, and less-luminous LBVs, which have initial masses of the order $M \sim 25 - 40\ M_{\odot}$ and which have presumably lost more than half of their initial mass during a previous RSG phase. Giant eruption LBVs, represented by the famous Galactic stars η Car and P Cygni, exhibit eruptions with visual magnitude changes of $2 - 3$ mag or more during which they can expel large amounts of material.

The terminal velocities of LBV winds are in the range of $100 - 250$ km s^{-1}, significantly lower than those of normal OB supergiants. LBV mass-loss rates are up to $10^{-5} - 10^{-4}\ M_{\odot}$ yr^{-1}, a factor of $10 - 100$ larger than those of normal supergiants. During their quiescent phases, LBVs lose mass likely via ordinary line-driving and the bistability mechanism is a good candidate to account for their transitional mass-loss variations (Vink 2021). The large mass-loss rates and giant eruptions observed in some LBVs suggest that also continuum-driven winds and/or explosions could play a role (Shaviv 1998, 2001; Owocki et al. 2004; Smith & Owocki 2006; Rest et al. 2012; Davidson & Humphreys 2012; Owocki & Shaviv 2016; González et al. 2022).

The morphology, kinematics, and chemical composition of their circumstellar nebulae trace the star's mass-loss history and evolution. Typically, LBV nebulae have sizes of $0.2 - 5$ pc, ionized masses of $1 - 4\ M_{\odot}$, and expansion velocities of several tenths to a few hundreds km s^{-1} (Weis 2003, see Figure 6). Bordiu et al. (2021) found that molecular gas may account for $> 30\%$ of the total mass lost around LBVs. At least 50% of the LBV nebulae are bipolar and several nebulae show in addition equatorial ring-like structures. To explain the observed nebular morphologies, a range of models have been proposed (see, e.g., Nota et al. 1995; Frank 1999; Frank et al. 1998; Owocki & Gayley 1997; Dwarkadas & Owocki 2002; Maeder & Desjacques 2001; Soker 2004). LBV nebulae are also unique laboratories to study the dust formation and dust survival in harsh

https://doi.org/10.1017/S1743921323000108 Published online by Cambridge University Press

conditions. The dust grains are unusually large and have an unusual composition compared to grains in the interstellar medium and the asymptotic giant branch stars. They may trace the cool outbursts or giant eruptions (Kochanek 2011) or they could have formed in a prior RSG phase (Waters et al. 1997).

It is yet unclear what causes the transitions of LBVs across the HR diagram and the giant LBV eruptions. Instabilities in the outer layers and core instabilities are proposed. The most prominent still discussed instability mechanisms are 1) radiation and turbulent pressure instabilities (Humphreys & Davidson 1984; Lamers 1986; Stothers 2003; Lamers & Fitzpatrick 1988; Ulmer & Fitzpatrick 1998), 2) ionization-induced dynamical instabilities (Maeder 1992; Stothers & Chin 1993, 1994, 1997; Glatzel & Kiriakidis 1993; Kiriakidis et al. 1993; Glatzel & Kiriakidis 1998; Lovekin & Guzik 2014; Jiang et al. 2018; Grassitelli et al. 2021), 3) deep rooted energy release or addition (Smith & Arnett 2014; Dessart et al. 2010; Smith & Arnett 2014; Meakin & Arnett 2007; Quataert & Shiode 2012; Shiode & Quataert 2014; Podsiadlowski et al. 2010; Smith & Arnett 2014; Dessart et al. 2010; Owocki et al. 2019). A single mechanism may be operating over a wide range of energy and mass, different mechanisms may produce the same observables, or several mechanisms may cooperate. Rotation (Langer 1998; Zhao & Fuller 2020; Shi & Fuller 2022), binary interaction (Kenyon & Gallagher 1985; Gallagher 1989; Smith 2011; Owocki et al. 2019; Quataert et al. 2016; Soker 2001, 2004, 2007; Kashi & Soker 2009; Smith et al. 2003; Koenigsberger 2004), and stellar mergers (Iben 1999; Portegies Zwart & van den Heuvel 2016; Hirai et al. 2021) may also play a crucial role in shaping the LBV phenomenon.

Eta Carinae. Eta Car is the prototype of the giant eruption LBVs. In the 1840/50s, it experienced an eruption during which it expelled up to 40 $M_{\odot}$ in 20 yr, which resulted in its Homunculus nebula. It is an eccentric, massive binary system with strong winds (the primary has a current mass-loss rate of $\sim 2.5 \times 10^{-4}$ $M_{\odot}$ yr^{-1}) and a phase-dependent wind-wind-collision (WWC) zone. The primary star is often classified as an LBV and the secondary is a WR or O-type star with a faster, less dense wind. Due to its dramatic nature and brightness, η Car has been extensively observed at all wavelength ranges and with a multitude of observing techniques (see Figure 7). Some selected recent studies are mentioned below.

Morphology and proper motions studies of the ejecta have been conducted at different wavelengths and spatial scales. Artigau et al. (2011) found with near-infrared adaptive optics imaging with the Near-Infrared Coronagraphic Imager (NICI) and the Nasmyth Adaptive Optics System (NAOS) Near-Infrared Imager and Spectrograph (CONICA), NaCO, a lobed pattern, the "butterfly nebula," outlined by bright Brγ and H_2 emission and light scattered by dust. Proper motions measured from the combined NICI and NaCO images together with radial velocities show that the knots and filaments that define the bright rims of the butterfly nebula were ejected at two different epochs corresponding approximately to the giant eruption and a second eruption around 1890. Abraham et al. (2020) presented images of η Car in the recombination lines H30α and He30α and the underlying continuum with 50 mas resolution (110 au), obtained with ALMA. They estimated the proper motions of nearby ejecta and derived ejection dates of 1952.6, 1957.1, and 1967.6, which are all close to periastron passages. Mehner et al. (2016) used large-scale integral field unit observations in the optical with the Multi Unit Spectroscopic Explorer (MUSE) at the VLT to reveal the detailed three-dimensional structure of its outer ejecta. Morpho-kinematic modeling of these ejecta were conducted with the code SHAPE (Steffen et al. 2010), which revealed a spatially coherent structure. Infrared long-baseline interferometry and synthesis imaging provides intensity and velocity distributions with milliarcsecond spatial resolution and offers opportunities to study the inner environment around η Car with a spatial resolution of a few au. Using

https://doi.org/10.1017/S1743921323000108 Published online by Cambridge University Press

Figure 7. Eta Car with VLT NACO (Credit: ESO).

the Multi AperTure mid-Infrared SpectroScopic Experiment (MATISSE) at the VLTI, Weigelt et al. (2021) performed Brα imaging of η Car's distorted wind. The asymmetries found are likely caused by the WWC. A fit of the observed continuum visibilities with the visibilities of a stellar wind CMFGEN model provides a diameter of the primary stellar wind of 2.84 ± 0.06 mas (6.54 ± 0.14 au). Analysis of the orbital phase-locked X-ray variability provides our most direct constraints on the momentum ratio of the two winds, the orbital eccentricity, and the shape of the colliding wind bow shock formed around the secondary star (Corcoran et al. 2017; Espinoza-Galeas et al. 2022). Observed orbit-to-orbit X-ray emission variations must arise from changes in the stellar wind properties of one or both of the stars. Explanations include significant changes in the primary star's wind mass-loss rate, variations in wind velocity, or wind clumping properties. At even higher energies, using γ-ray *FERMI-LAT* observations, Martí-Devesa & Reimer (2021) found that the wind collision region of this system is perturbed from orbit to orbit, affecting particle transport within the shock.

2.6. *Wolf-Rayet stars.*

Classical WR stars are generally assumed to be evolved, helium-burning massive stars that have lost most of their hydrogen envelope through prior mass loss, exposing the helium core. They are the progenitor candidates of SN Ib/Ic and long-duration gamma ray bursts. Classification as a WR star is performed based on spectroscopic terminology, i.e., based on the presence of strong and broad emission lines which are produced by strong winds. Such spectra can also originate in objects with very large initial stellar mass and luminosity or in binary-stripped objects (Stanway et al. 2016; Götberg et al.

https://doi.org/10.1017/S1743921323000108 Published online by Cambridge University Press

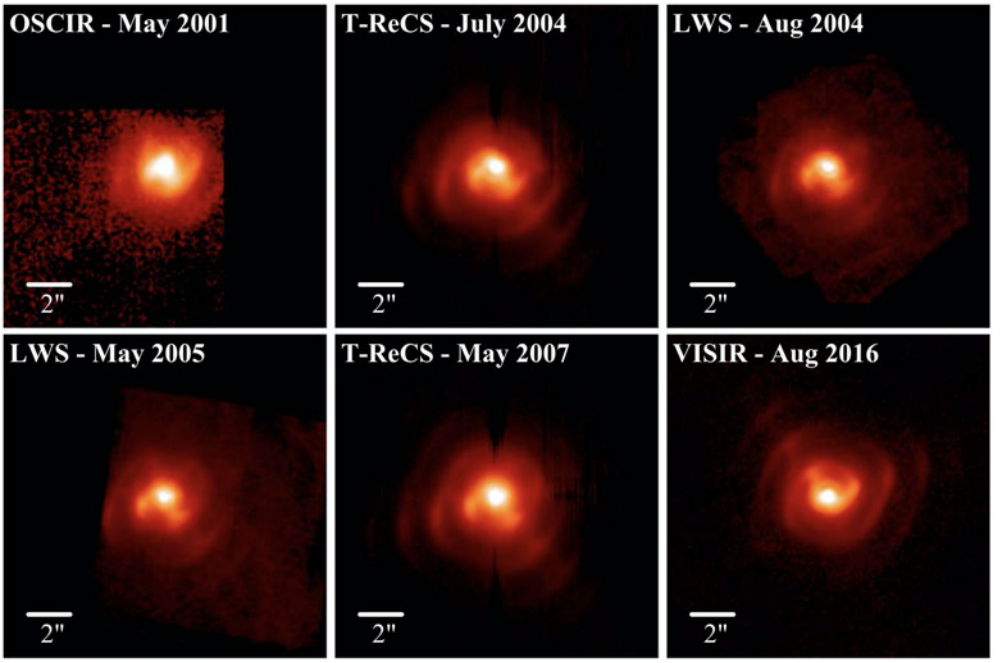

Figure 8. *N*-band images of WR 112 (Figure from Lau et al. 2020).

2020). Thus, this stellar group may include objects still in their core hydrogen-burning phase of evolution. The mechanism of the hydrogen-envelope stripping and how it varies with metallicity is a long-standing unsolved issue. It is not clear if all single O-type stars can evolve to become a WR star, or only those in interacting binaries.

Classical WR stars have strong winds with large mass-loss rates (Crowther 2007), driven by radiation pressure and typically a factor of 10 larger than O-star winds with the same luminosity. The wind strength is found to be dependent on the Fe abundance, but with a metallicity dependence that is less steep than for OB stars (Vink & de Koter 2005). Empirical mass-loss rates have been derived from radio emission, optical emission line equivalent width relationships, and spectral analysis of optical and near-infrared data using non-LTE radiative transfer codes like CMFGEN (Nugis & Lamers 2000; Bestenlehner et al. 2014). Sander et al. (2019) and Hamann et al. (2019) revised the correlations between the mass-loss rate and the luminosity for WC, WO, and WN stars based on Gaia DR2 data. Sander et al. (2019) found for WC and WO stars luminosities ranging from $log\ L/L_{\odot} = 4.9 - 6.0$, which indicates that the WC stars are likely formed from a broader initial mass range than previously assumed. They also obtained mass-loss rates ranging between $log\ \dot{M} = -5.1$ and -4.1, with $\dot{M} \propto L^{0.68}$. Hamann et al. (2019) found that the correlations between mass-loss rate and luminosity show a large scatter for the WN stars, with shallower slopes than found previously.

In colliding wind systems, the enhanced density in the WWC produces favorable conditions for dust formation. Combined with the Coriolis force due to the orbital motion, this gives rise to so-called pinwheel nebulae that are characterized by a dust plume following an Archimedian spiral pattern.

WR 112. WR 112 is a dust-forming late-type carbon-rich Wolf–Rayet (WC)–OB binary system with a dusty circumstellar nebula that exhibits a complex asymmetric morphology, which traces the orbital motion and dust formation in the colliding winds of the central binary (Figure 8). Lau et al. (2017) presented high spatial resolution

https://doi.org/10.1017/S1743921323000108 Published online by Cambridge University Press

mid-infrared images of its nebula obtained with VLT VISIR over a period of 9 yr. The observations revealed a morphology resembling a series of arc-like filaments and broken shells, that the authors interpreted as a consecutive series of stagnant dust shells exhibiting no proper motion, which may have formed in the outflow during a previous red or yellow supergiant phase. Lau et al. (2020) presented a multi-epoch proper motion and morphological analysis of the circumstellar dust using seven high spatial resolution N-band imaging observations spanning almost 20 yr, leading to a revision of their previous morphological interpretation of the geometry. They found evidence of proper motion of the circumstellar dust consistent with a nearly edge-on spiral with a period of $P \sim 20$ yr. They spectroscopically derived a terminal stellar wind velocity of $v = 1230 \pm 260$ km s^{-1}. Fitting optically thin dust SED models, they determined a dust production rate of $\dot{M}_{\rm dust} = 2.7^{1.0}_{1.3} \times 10^{-6}\ M_{\odot}$ yr^{-1}, which demonstrates that WR 112 is one of the most prolific dust-making WC systems known.

3. Summary

There has been much observational progress in the past decade in our understanding of the mass loss in the most massive stars. This can be attributed to ground-based 10-m class observatories equipped with multi-object spectrographs, AO, and interferometric instrumentation, and space-based observatories with capabilities in the UV, infrared, X-ray.

There are still many unsolved questions related to mass loss and outflows in the most massive stars. Observational measurements have large uncertainties. It is also not yet established how rotation and binarity affect the mass loss. The majority of massive stars are binary systems that will at one point in their evolution interact and the finding of relatively low steady wind mass-loss rates has shifted the attention to binary interaction that can create and shape outflows.

Due to their brightness, massive stars are excellent targets for almost any observing technique and wavelength range, enabling a multi-wavelength approach that provides different diagnostics and consistency checks. Upcoming large survey missions (e.g., Euclid, Roman, Rubin) will provide an improved census of evolved massive stars, massive star transients, and SN precursors. High-multiplex spectroscopic surveys (e.g., 4MOST, MOONS) will allow their follow-up and detailed analysis of their stellar winds and outflows.

References

Abraham, Z., Beaklini, P. P. B., Cox, P., Falceta-Gonçalves, D., & Nyman, L.-Å. 2020, MNRAS, 499, 2493
Aret, A., Kraus, M., Muratore, M. F., & Borges Fernandes, M. 2012, MNRAS, 423, 284
Arroyo-Torres, B., Wittkowski, M., Chiavassa, A., et al. 2015, A&A, 575, A50
Artigau, É., Martin, J. C., Humphreys, R. M., et al. 2011, AJ, 141, 202
Bally, J., Ginsburg, A., Silvia, D., & Youngblood, A. 2015, A&A, 579, 130
Bally, J. 2016, ARA&A, 54, 491
Bally, J., Ginsburg, A., Arce, H., et al. 2017, ApJ, 837, 60
Bally, J., Ginsburg, A., Forbrich, J., & Vargas-González, J. 2020, ApJ, 889, 178
Bally, J., & Zinnecker, H. 2005, AJ, 129, 2281
Baron, F., Monnier, J. D., Kiss, L. L., et al. 2014, ApJ, 785, 46
Beasor, E. R., Davies, B., Smith, N., et al. 2020, MNRAS, 492, 5994
Bestenlehner, J. M., Gräfener, G., Vink, J. S., et al. 2014, A&A, 570, A38
Björklund, R., Sundqvist, J. O., Puls, J., & Najarro, F. 2021, A&A, 648, A36
Bordiu, C., Bufano, F., Cerrigone, L., et al. 2021, MNRAS, 500, 5500
Bouret, J. C., Martins, F., Hillier, D. J., et al. 2021, A&A, 647, A134
Brennan, S. J., Fraser, M., Johansson, J., et al. 2022, MNRAS, 513, 5666

https://doi.org/10.1017/S1743921323000108 Published online by Cambridge University Press

Carrasco-González, C., Sanna, A., Rodríguez-Kamenetzky, A., et al. 2021, ApJL, 914, L1
Castor, J. I., Abbott, D. C., & Klein, R. I. 1975, ApJ, 195, 157
Corcoran, M. F., Liburd, J., Morris, D., et al. 2017, ApJ, 838, 45
Cortes, P. C., Le Gouellec, V. J. M., Hull, C. L. H., et al. 2021, ApJ, 907, 94
Crowther, P. A. 2007, ARA&A, 45, 177
Cunningham, N. J., Moeckel, N., & Bally, J. 2009, ApJ, 692, 943
Davidson, K., & Humphreys, R. M. 2012, Nature, 486, E1
de Jager, C. 1998, A&A Rev., 8, 145
Decin, L., Hony, S., de Koter, A., et al. 2006, A&A, 456, 549
Decin, L., Richards, A. M. S., Millar, T. J., et al. 2016, A&A, 592, A76
Dessart, L., Livne, E., & Waldman, R. 2010, MNRAS, 405, 2113
Dharmawardena, T. E., Mairs, S., Scicluna, P., et al. 2020, ApJL, 897, L9
Domiciano de Souza, A., Kervella, P., Bendjoya, P., & Niccolini, G. 2008, A&A, 480, L29
Domiciano de Souza, A., Driebe, T., Chesneau, O., et al. 2007, A&A, 464, 81
Dressing, C. D., & Charbonneau, D. 2013, ApJ, 767, 95
Dupree, A. K., Strassmeier, K. G., Matthews, L. D., et al. 2020, ApJ, 899, 68
Dwarkadas, V. V., & Owocki, S. P. 2002, ApJ, 581, 1337
Espinoza-Galeas, D., Corcoran, M. F., Hamaguchi, K., et al. 2022, ApJ, 933, 136
Evans, C. J., Taylor, W. D., Hénault-Brunet, V., et al. 2011, A&A, 530, A108
Foley, R. J., Berger, E., Fox, O., et al. 2011, ApJ, 732, 32
Frank, A. 1999, NewA, 43, 31
Frank, A., Ryu, D., & Davidson, K. 1998, ApJ, 500, 291
Fullerton, A. W., Massa, D. L., & Prinja, R. K. 2006, ApJ, 637, 1025
Gallagher, J. S. 1989, in ASSL, Vol. 157, IAU Colloq. 113: Physics of Luminous Blue Variables, ed. K. Davidson, A. F. J. Moffat, & H. J. G. L. M. Lamers, 185
Glatzel, W., & Kiriakidis, M. 1993, MNRAS, 263, 375
Glatzel, W., & Kiriakidis, M. 1998, MNRAS, 295, 251
González, R. F., Zapata, L. A., Raga, A. C., et al. 2022, A&A, 659, A168
Gordon, M. S., Jones, T. J., Humphreys, R. M., et al. 2019, AJ, 157, 57
Götberg, Y., de Mink, S. E., McQuinn, M., et al. 2020, A&A, 634, A134
Gräfener, G., Koesterke, L., & Hamann, W. R. 2002, A&A, 387, 244
Grassitelli, L., Langer, N., Mackey, J., et al. 2021, A&A, 647, A99
Groh, J. H. 2017, Philos. Trans. Royal Soc. A, 375, 20170219
Groh, J. H., Meynet, G., & Ekström, S. 2013, A&A, 550, L7
Habing, H. J. 1996, A&A Rev., 7, 97
Hamann, W. R., Gräfener, G., Liermann, A., et al. 2019, A&A, 625, A57
Haubois, X., Perrin, G., Lacour, S., et al. 2009, A&A, 508, 923
Henney, W. J., & Arthur, S. J. 2019, MNRAS, 489, 2142
Hillier, D. J., & Miller, D. L. 1998, ApJ, 496, 407
Hirai, R., Podsiadlowski, P., Owocki, S. P., Schneider, F. R. N., & Smith, N. 2021, MNRAS, 503, 4276
Humphreys, R. M., & Davidson, K. 1984, Science, 223, 243
Humphreys, R. M., Smith, N., Davidson, K., Jones, T. J., et al. 1997, AJ, 114, 2778
Humphreys, R. M., Davidson, K., Hahn, D., et al. 2017, ApJ, 844, 40
Humphreys, R. M., Davidson, K., Richards, A. M. S., et al. 2021, AJ, 161, 98
Humphreys, R. M., & Jones, T. J. 2022, AJ, 163, 103
Iben, Jr., I. 1999, in ASP Conf. Ser., Vol. 179, Eta Carinae at The Millennium, ed. J. A. Morse, R. M. Humphreys, & A. Damineli, 367
Janson, M., Gratton, R., Rodet, L., et al. 2021, Nature, 600, 231
Jiang, Y.-F., Cantiello, M., Bildsten, L., et al. 2018, Nature, 561, 498
Josselin, E., & Plez, B. 2007, A&A, 469, 671
Justham, S., Podsiadlowski, P., & Vink, J. S. 2014, ApJ, 796, 121
Kamiński, T. 2019, A&A, 627, A114
Kashi, A., & Soker, N. 2009, NewA, 14, 11

Kenyon, S. J., & Gallagher, J. S., I. 1985, ApJ, 290, 542
Kervella, P., Perrin, G., Chiavassa, A., et al. 2011, A&A, 531, A117
Kervella, P., Decin, L., Richards, A. M. S., et al. 2018, A&A, 609, A67
Kiriakidis, M., Fricke, K. J., & Glatzel, W. 1993, MNRAS, 264, 50
Kobulnicky, H. A., Chick, W. T., & Povich, M. S. 2019, AJ, 158, 73
Kochanek, C. S. 2011, ApJ, 743, 73
Koenigsberger, G. 2004, RMxAA, 40, 107
Koumpia, E., Oudmaijer, R. D., Graham, V., et al. 2020, A&A, 635, A183
Koumpia, E., Oudmaijer, R. D., de Wit, W. -J., et al. 2022, MNRAS, 515, 2766
Kraus, M., Borges Fernandes, M., & de Araújo, F. X. 2007, A&A, 463, 627
Kraus, M., Borges Fernandes, M., & de Araújo, F. X. 2010, A&A, 517, A30
Kraus, M., Oksala, M. E., Nickeler, D. H., et al. 2013, A&A, 549, A28
Kraus, M., Cidale, L. S., Arias, M. L., et al. 2016, A&A, 593, A112
Kravchenko, K., Jorissen, A., Van Eck, S., et al. 2021, A&A, 650, L17
Kudritzki, R.-P., & Puls, J. 2000, ARA&A, 38, 613
Lagadec, E., Zijlstra, A. A., Oudmaijer, R. D., et al. 2011, A&A, 534, L10
Lamers, H. J. G. L. M. 1986, A&A, 159, 90
Lamers, H. J. G. L. M., & Fitzpatrick, E. L. 1988, ApJ, 324, 279
Lamers, H. J. G. L. M., Nota, A., Panagia, N., Smith, L. J., & Langer, N. 2001, ApJ, 551, 764
Lamers, H. J. G. L. M., Snow, T. P., & Lindholm, D. M. 1995, ApJ, 455, 269
Langer, N. 1998, A&A, 329, 551
Lau, R. M., Hankins, M. J., Schödel, R., et al. 2017, ApJL, 835, L31
Lau, R. M., Hankins, M. J., Han, Y., et al. 2020, ApJ, 900, 190
Liimets, T., Kraus, M., Moiseev, A., et al. 2022, Galaxies, 10, 41
Lovekin, C. C., & Guzik, J. A. 2014, MNRAS, 445, 1766
Lucy, L. B., & Solomon, P. M. 1970, ApJ, 159, 879
Maeder, A. 1992, in Instabilities in Evolved Super- and Hypergiants, ed. C. de Jager & H. Nieuwenhuijzen, 138
Maeder, A., & Desjacques, V. 2001, A&A, 372, L9
Maravelias, G., Kraus, M., Cidale, L. S., et al. 2018, MNRAS, 480, 320
Marcolino, W. L. F., Bouret, J. C., Rocha-Pinto, H. J., Bernini-Peron, M., & Vink, J. S. 2022, MNRAS, 511, 5104
Martí-Devesa, G., & Reimer, O. 2021, A&A, 654, A44
Matt, S., Frank, A., & Blackman, E. G. 2006, ApJL, 647, L45
Meakin, C. A., & Arnett, D. 2007, ApJ, 667, 448
Mehner, A., Davidson, K., Humphreys, R. M., et al. 2015, A&A, 578, A122
Mehner, A., Steffen, W., Groh, J. H., et al. 2016, A&A, 595, A120
Millour, F., Meilland, A., Chesneau, O., et al. 2011, A&A, 526, A107
Mokiem, M. R., de Koter, A., Evans, C. J., et al. 2006, A&A, 456, 1131
Mokiem, M. R., de Koter, A., Vink, J. S., et al. 2007a, A&A, 473, 603
Mokiem, M. R., de Koter, A., Evans, C. J., et al. 2007b, A&A, 465, 1003
Monnier, J. D., Millan-Gabet, R., Tuthill, P. G., et al. 2004, ApJ, 605, 436
Montargès, M., Homan, W., Keller, D., et al. 2019, MNRAS, 485, 2417
Montargès, M., Cannon, E., Lagadec, E., et al. 2021, Nature, 594, 365
Nota, A., Livio, M., Clampin, M., & Schulte-Ladbeck, R. 1995, ApJ, 448, 788
Nugis, T., & Lamers, H. J. G. L. M. 2000, A&A, 360, 227
O'Gorman, E., Vlemmings, W., Richards, A. M. S., et al. 2015, A&A, 573, L1
Ohnaka, K. 2014, A&A, 568, A17
Oudmaijer, R. D., Groenewegen, M. A. T., Matthews, H. E., et al. 1996, MNRAS, 280,1062
Owocki, S. P., & Gayley, K. G. 1997, in Astron. Soc. Pac. Conf. Ser., Vol. 120, Luminous Blue Variables: Massive Stars in Transition, ed. A. Nota & H. Lamers, 121
Owocki, S. P., Gayley, K. G., & Shaviv, N. J. 2004, ApJ, 616, 525
Owocki, S. P., Hirai, R., Podsiadlowski, P., & Schneider, F. R. N. 2019, MNRAS, 485, 988
Owocki, S. P., & Shaviv, N. J. 2016, MNRAS, 462, 345

Petrov, B., Vink, J. S., & Gräfener, G. 2016, MNRAS, 458, 1999
Podsiadlowski, P., Ivanova, N., Justham, S., & Rappaport, S. 2010, MNRAS, 406, 840
Poppenhaeger, K., Ketzer, L., & Mallonn, M. 2021, MNRAS, 500, 4560
Portegies Zwart, S. F., & van den Heuvel, E. P. J. 2016, MNRAS, 456, 3401
Porter, A., Blundell, K., & Lee, S. 2022, MNRAS, 509, 1720
Puls, J., Urbaneja, M. A., Venero, R., et al. 2005, A&A, 435, 669
Puls, J., Vink, J. S., & Najarro, F. 2008, A&A Rev., 16, 209
Puls, J., Kudritzki, R. P., Herrero, A., et al. 1996, A&A, 305, 171
Quataert, E., Fernández, R., Kasen, D., Klion, H., & Paxton, B. 2016, MNRAS, 458, 1214
Quataert, E., & Shiode, J. 2012, MNRAS, 423, L92
Ramachandran, V., Hamann, W. R., Oskinova, L. M., et al. 2019, A&A, 625, A104
Ramírez-Agudelo, O. H., Sana, H., de Koter, A., et al. 2017, A&A, 600, A81
Reffert, S., Bergmann, C., Quirrenbach, A., Trifonov, T., & Künstler, A. 2015, A&A, 574, A116
Reggiani, M., Rainot, A., Sana, H., et al. 2022, A&A, 660, A122
Rest, A., Prieto, J. L., Walborn, N. R., et al. 2012, Nature, 482, 375
Rickard, M. J., Hainich, R., Hamann, W. R., et al. 2022, arXiv e-prints, arXiv:2207.09333
Rivinius, T., Carciofi, A. C., & Martayan, C. 2013, A&A Rev., 21, 69
Rosen, A. L., & Krumholz, M. R. 2020, AJ, 160, 78
Rubio-Díez, M. M., Sundqvist, J. O., Najarro, F., et al. 2022, A&A, 658, A61
Sander, A. A. C., Hamann, W. R., Todt, H., Hainich, R., & Shenar, T. 2017, A&A, 603, A86
Sander, A. A. C., Hamann, W. R., Todt, H., et al. 2019, A&A, 621, A92
Shaviv, N. J. 1998, ApJL, 494, L193
Shaviv, N. J. 2001, MNRAS, 326, 126
Shenar, T., Sana, H., Marchant, P., et al. 2021, A&A, 650, A147
Shenoy, D., Humphreys, R. M., Jones, T. J., et al. 2016, AJ, 151, 51
Shenoy, D. P., Jones, T. J., Humphreys, R. M., et al. 2013, AJ, 146, 90
Shi, Y., & Fuller, J. 2022, MNRAS, 513, 1115
Shiode, J. H., & Quataert, E. 2014, ApJ, 780, 96
Smith, L. J., Nota, A., Pasquali, A., et al. 1998, ApJ, 503, 278
Smith, L. J., Stroud, M. P., Esteban, C., & Vilchez, J. M. 1997, MNRAS, 290, 265
Smith, N. 2011, MNRAS, 415, 2020
Smith, N. 2014, ARA&A, 52, 487
Smith, N. 2017, Philos. Trans. Royal Soc. A, 375, 20160268
Smith, N., Andrews, J. E., Filippenko, A. V., et al. 2022, MNRAS, 515, 71
Smith, N., & Arnett, W. D. 2014, ApJ, 785, 82
Smith, N., Davidson, K., Gull, T. R., Ishibashi, K., & Hillier, D. J. 2003, ApJ, 586, 432
Smith, N., & Owocki, S. P. 2006, ApJL, 645, L45
Smith, N., Miller, A., Li, W., et al. 2010, AJ, 139, 1451
Soker, N. 2001, MNRAS, 325, 584
Soker, N. 2004, ApJ, 612, 1060
Soker, N. 2007, ApJ, 661, 482
Squicciarini, V., Gratton, R., Janson, M., et al. 2022, A&A, 664, 9
Stanway, E. R., Eldridge, J. J., & Becker, G. D. 2016, MNRAS, 456, 485
Steffen, W., Koning, N., Wenger, S., Morisset, C. & Magnor, M. 2010, IEEE Transactions on Visualization and Computer Graphics, Vol. 17, Issue 4, 454
Stothers, R. B. 2003, ApJ, 589, 960
Stothers, R. B., & Chin, C.-W. 1993, ApJL, 408, L85
Stothers, R. B., & Chin, C.-W. 1994, ApJL, 426, L43
Stothers, R. B., & Chin, C.-W. 1997, ApJ, 489, 319
Taniguchi, D., Yamazaki, K., & Uno, S. 2022, NatAs, 6, 930
Thirumalai, A., & Heyl, J. S. 2012, MNRAS, 422, 1272
Tiffany, C., Humphreys, R. M., Jones, T. J., & Davidson, K. 2010, AJ, 140, 339
Ulmer, A., & Fitzpatrick, E. L. 1998, ApJ, 504, 200
Ustamujic, S., Orlando, S., Miceli, M., et al. 2021, A&A, 654, A167

Vieira, R. G., Carciofi, A. C., Bjorkman, J. E., et al. 2017, MNRAS, 464, 3071
Vink, J. S. 2021, arXiv e-prints, arXiv:2109.08164
Vink, J. S., & de Koter, A. 2005, A&A, 442, 587
Vink, J. S., de Koter, A., & Lamers, H. J. G. L. M. 2001, A&A, 369, 574
Vlemmings, W. H. T., Khouri, T., Martí-Vidal, I., et al. 2017, A&A, 603, A92
Wallström, S. H. J., Muller, S., Lagadec, E., et al. 2015, A&A, 574, A139
Wallström, S. H. J., Lagadec, E., Muller, S., et al. 2017, A&A, 597, A99
Waters, L. B. F. M., Morris, P. W., Voors, R. H. M., & Lamers, H. J. G. L. M. 1997, in Astron. Soc. Pac. Conf. Ser., Vol. 120, Luminous Blue Variables: Massive Stars in Transition, ed. A. Nota & H. Lamers, 326
Weigelt, G., Hofmann, K. H., Schertl, D., et al. 2021, A&A, 652, A140
Weis, K. 2003, A&A, 408, 205
Weis, K. 2011, Proc. Int. Astron. Union, IAUS 272, Active OB stars: structure, evolution, mass loss, and critical limits, ed. C. Neiner, G. Waade, G. Meynet & G. Peters, 372
Wheelwright, H. E., de Wit, W. J., Weigelt, G., Oudmaijer, R. D., & Ilee, J. D. 2012, A&A, 543, A77
Wittkowski, M., Hauschildt, P. H., Arroyo-Torres, B., & Marcaide, J. M. 2012, A&A, 540, L12
Xu, D., Offner, S. S. R., Gutermuth, R., Kong, S., & Arce, H. G. 2022, ApJ, 926, 19
Zhao, X., & Fuller, J. 2020, MNRAS, 495, 249
Zickgraf, F. J., Wolf, B., Stahl, O., Leitherer, C., & Klare, G. 1985, A&A, 143, 421